

Real-time Melt Pool Depth Estimation and Control During Metal-directed Energy Deposition for Porosity Reduction

Ikgeun Jeon

Korea Advanced Institute of Science and Technology

Peipei Liu

Korea Advanced Institute of Science and Technology

Hoon Sohn (✉ hoonsohn@kaist.ac.kr)

Korea Advanced Institute of Science and Technology

Research Article

Keywords: Melt pool depth, Online monitoring, Feedback control, Artificial neural network, Metal-directed energy deposition, Additive manufacturing

Posted Date: January 18th, 2022

DOI: <https://doi.org/10.21203/rs.3.rs-1240455/v1>

License:  This work is licensed under a Creative Commons Attribution 4.0 International License.

[Read Full License](#)

Real-time melt pool depth estimation and control during metal-directed energy deposition for porosity reduction

Ikgeun Jeon^a, Peipei Liu^{a, b}, and Hoon Sohn^{a, b*}

^a Department of Civil and Environmental Engineering, Korea Advanced Institute of Science and Technology (KAIST), Daehakro 291, Yuseong-gu, Daejeon 34141, Republic of Korea

^b Center for 3D Printing Nondestructive Testing, Korea Advanced Institute of Science and Technology (KAIST), Daehakro 291, Yuseong-gu, Daejeon 34141, Republic of Korea

*Corresponding author: hoonsohn@kaist.ac.kr

Abstract¹

Porosity is one of the most critical defects in additive manufacturing (AM). Although porosity formation is significantly influenced by the melt pool depth (MPD), MPD estimation and control during AM is difficult to realize. In this study, a real-time MPD estimation and control system was developed to reduce porosity formation during metal-directed energy deposition (DED). First, the width, length, height, and profile slope of the melt pool were measured using an infrared camera and a line scanner during the DED process. Thereafter, an artificial neural network (ANN) was trained and adopted to estimate the MPD in real time. A feedback control system, which adjusts the power of the printing laser, was developed to instantaneously minimize the discrepancy between the estimated MPD value and the set MPD value. The effectiveness of the proposed system for porosity reduction was validated by inspecting the printed metal components using X-ray microscopy. The porosity of the components printed with the proposed system was 81% reduced in comparison with the uncontrolled parts.

Keywords

Melt pool depth, Online monitoring, Feedback control, Artificial neural network, Metal-directed energy deposition, Additive manufacturing

¹ Abbreviations:

AM: Additive manufacturing; MPD: Melt pool depth; DED: Directed energy deposition; ANN: Artificial neural network; VED: Volumetric energy density; PID: Proportional–integral–derivative.

1. Introduction

Metal additive manufacturing (AM) is currently an important rapid prototyping technique. Directed energy deposition (DED) is a representative method of metal AM and provides the advantages of large-scale manufacturing, multi-material fabrication, and a high build rate [1, 2]. Although new printing materials and effective printing methods have been developed for the DED process, quality uncertainty is a major problem due to the lack of online monitoring and quality control techniques [3].

Porosity is one of the most critical defects that determine the part quality of the DED process. For example, porosity influences mechanical properties such as stiffness, strength, toughness, and corrosion resistance [4–6]. Moreover, porosity is related to fatigue performance, given that cracks are generally initiated at the tips of pores [7]. Therefore, reducing porosity is a major objective for improving part quality in the DED process.

In general, porosity formation is significantly influenced by the melt pool depth (MPD), which is defined as the distance from the deposited layer surface to the lowest point of the melt pool [8–10]. The MPD determines the type of porosity: lack-of-fusion and gas entrapment as shown in Fig. 1. Lack of fusion is indicated by sharp crack-like pores with a typical size of 100–150 μm [11]. This type of porosity is caused by an insufficient overlap between layers due to small MPDs. Gas entrapment is indicated by spherical pores with a typical size of 10–50 μm [12]. A large MPD causes gas entrapment, given that the gases in the melt pool cannot readily escape before solidification.

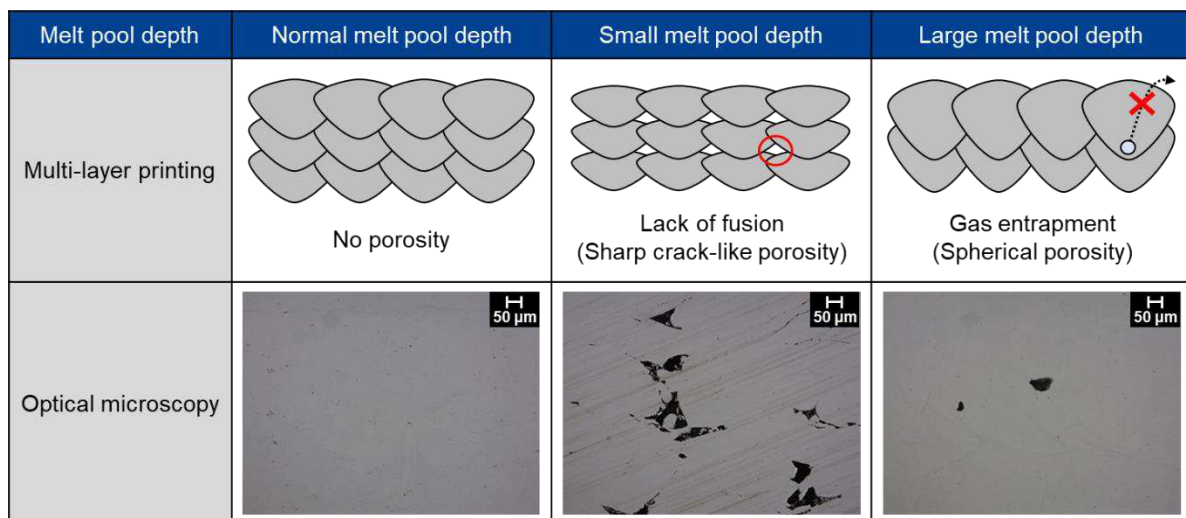


Fig. 1. Melt pool depth (MPD) and porosity

Given that the MPD cannot be directly measured, several methods have been designed to reduce porosity without obtaining the MPD. Volumetric energy density (VED), which is a function of the laser power, scanning speed, and layer height, was used to examine porosity [13–15]. For example, Kasperovich *et al.* investigated the correlation between the VED and porosity to determine the optimal VED range for the fabrication of fully dense Ti-6Al-4V parts [16]. Although the VED can examine the porosity, iterative testing was required to establish a new VED–porosity relationship with respect to the printing parameter. Moreover, a hot isostatic pressing was applied to remove the pores near the surface [17, 18], and a printing laser was oscillated to reduce porosity by accelerating the heat flow inside the melt pool [19, 20]. However, the abovementioned methods cannot be used to accurately control porosity during multi-layer printing, as they do not consider heat accumulation or the complex geometries of the printed parts.

To solve this problem, several studies were conducted to estimate the MPD of multi-layer printing. The MPD was estimated by combining the melt pool width-to-depth ratio obtained from an analytical model and the melt pool width measured using a coaxial camera [21]. Furthermore, an ultra-fast synchrotron X-ray technique was used to observe the flow dynamics and MPD in keyhole mode printing [22, 23]. However, the data processing of both methods was performed offline, i.e., the MPD cannot be estimated online.

In this study, a real-time MPD estimation and control system was developed for porosity reduction in the DED process. First, the width, length, height, and profile slope of the melt pool were measured using an infrared camera and a line scanner during the DED process. The infrared camera was used to measure the width and length of the melt pool, and the line scanner was used to measure the height and slope of the melt pool. These extracted melt pool features were used as the input of an artificial neural network (ANN), and the MPD was estimated in real-time with an accuracy of 23 μm . Subsequently, a developed feedback control system was used to adjust the power of the printing laser to maintain the MPD at the set value. With reference to the available literature, this study represents the first development of an MPD estimation and control system for porosity reduction during the DED process. The novelty of this study can be summarized as follows. (1) The MPD was estimated online using a melt pool monitoring system composed of an infrared camera, a line scanner, and an ANN. (2) A feedback control system for the printing laser power was developed to minimize the

discrepancy between the estimated MPD and the set MPD. (3) It was experimentally validated that real-time MPD control resulted in significant porosity reduction. (4) The performance of the developed system was compared with those of existing laser power control systems based on energy density or melt pool width measurements.

2. Materials and methods

2.1. Online melt pool monitoring

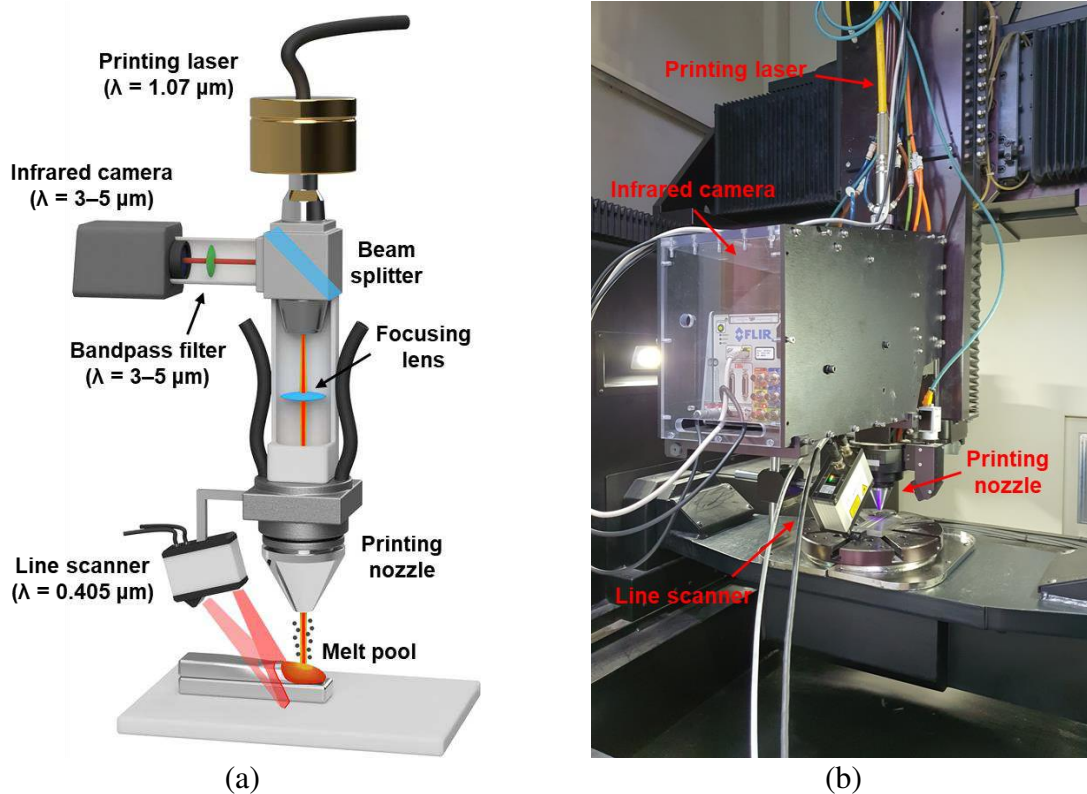


Fig. 2. Proposed online melt pool monitoring module integrated into a directed energy deposition (DED) machine: (a) schematic and (b) actual image

In this study, the DED process was carried out using an InssTek MX-400 machine equipped with an ytterbium fiber printing laser. This printing laser has a maximum power of 1 kW, a wavelength of 1.07 μm , and spot diameter of 800 μm at a nozzle operating distance of 9 mm. Stainless steel 316L powder (KOS Ltd.) with a particle size distribution of D10 = 59 μm , D50 = 84.5 μm , and D90 = 122.0 μm was used for the experiments. The powder feed rate was 5.2 g/min. The carrier and shield gas were 99.99 % pure Argon with flow rates of 3 L/min and 5 L/min, respectively. The substrate was made of the same material as the powder, and the dimensions were 100 mm \times 50 mm \times 10 mm.

As described in Fig. 2, an online melt pool monitoring module composed of an infrared camera (X8500sc, FLIR Systems, Inc.) and a line scanner (scanCONTROL 3000-25/BL, Micro-Epsilon, Inc.) was developed to extract the melt pool features. Initially, the thermal radiation from the melt pool passed through a beam splitter and a bandpass filter. The beam splitter reflected the melt pool radiation toward the infrared camera, and the bandpass filter reduced the radiation intensity to prevent damage to the infrared camera. The infrared camera detected radiation with a wavelength of 3–5 μm and was not influenced by the printing laser with a wavelength of 1.07 μm . Additionally, the coaxial installation of the infrared camera had the advantage of a steady image resolution over the off-axis setting, given that the infrared camera measured the melt pool during its movement with the printing nozzle.

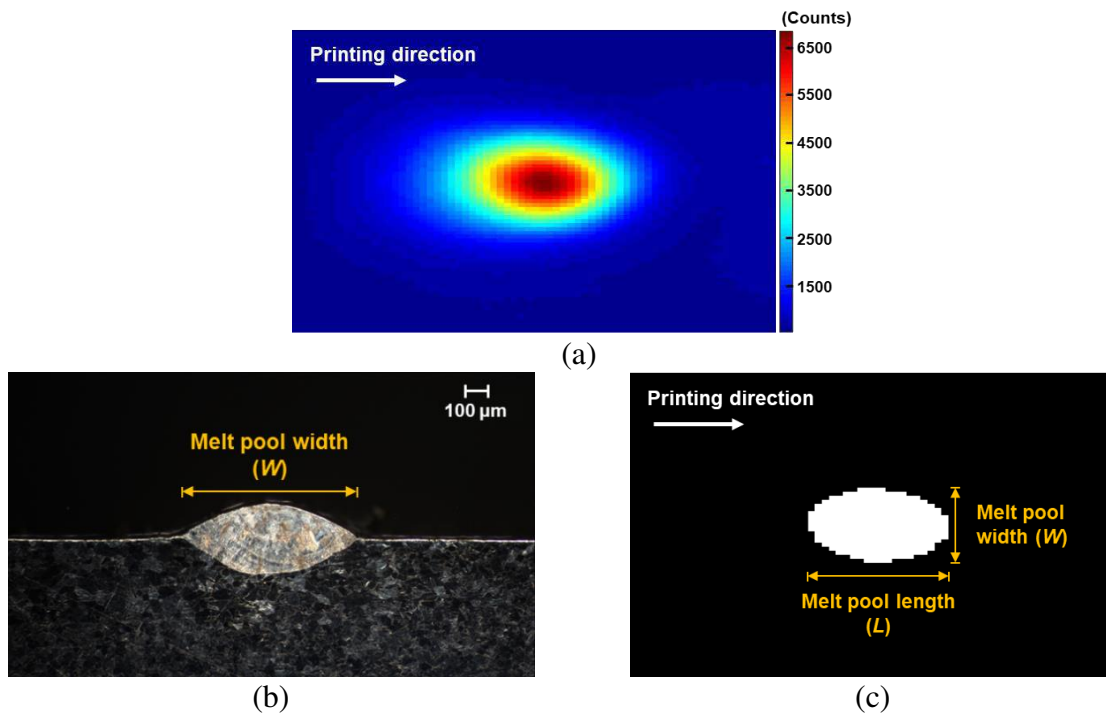


Fig. 3. Coaxial thermography measurement during DED process: (a) obtained thermal image, (b) optical microscopy image of cross-sectioned single-track, and (c) extraction of melt pool boundary

Fig. 3(a) presents a thermal image captured using the infrared camera during the DED process. The image had 320×256 pixels with a resolution of 55 μm and was captured at a frame rate of 200 Hz. The count value of the image pixel represents the intensity of thermal radiation. In general, the count value and actual temperature value are calibrated in consideration of the emissivity of the measuring material. However, for the DED process, it

was difficult to obtain the emissivity of the melt pool due to the metal powder and argon gas supplied to the melt pool. Subsequently, a calibration test was performed to identify the melting temperature from the thermal image without considering emissivity. First, a thermal image of single-track printing was captured as shown in Fig. 3(a). The single-track was cross-sectioned and the melt pool boundary was identified via optical microscopy (GX53, OLYMPUS, Inc.), as presented in Fig. 3(b). Based on the micro-analysis, the count value of the pixel located at the melt pool boundary was 4500, which represents the melting temperature. Consequently, pixels with a count value of 4500 or higher were defined as the melt pool, and the width (W) and length (L) of the melt pool were extracted as shown in Fig. 3(c).

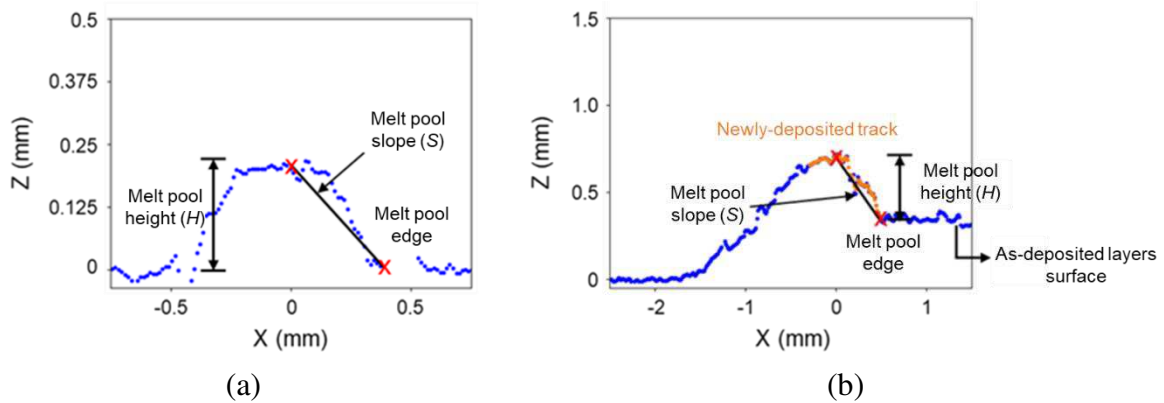


Fig. 4. Line scanning measurement during (a) single-track and (b) multi-layer printing

The line scanner, which is referred to as a profile sensor, was used to measure the melt pool height and slope. A line scanner measures the two-dimensional profile of a target surface based on the laser triangulation principle [24]. In this study, the line scanner had resolutions of 12 μm and 1.5 μm in the horizontal and vertical directions, respectively. The width of the profile line was 14 mm with a frame rate of 100 Hz. To avoid the powder spatter around the deposited area, the profile line was located 27 mm from the printing laser, as illustrated in Fig. 2.

Fig. 4(a) presents the line scanning measurement during single-track printing. The printing laser was positioned at the zero value of the X-axis, which was perpendicular to the printing direction. The zero value of the Z-axis represents the substrate surface. Given that the melt pool was created around the printing laser, the maximum Z value in the range of -0.5 to 0.5 mm along the X-axis was defined as the melt pool height (H). Moreover, the melt pool edge

was defined as a measured point of intersection between the melt pool and the substrate in the positive X direction. Thereafter, the melt pool slope (S) was defined as the slope between melt pool edge and a measured point with an X value of zero.

The line scanning measurement in the multi-layer printing is shown in Fig. 4(b). In this case, the melt pool edge was defined as the intersection between the melt pool and the as-deposited layers surface. Thereafter, the melt pool height (H) was defined as the vertical distance from the as-deposited layers surface to the maximum Z value in the range of -0.5 mm to 0.5 mm along the X-axis. The melt pool slope (S) was defined the same as that for single-track printing.

2.2. The MPD estimation using an ANN

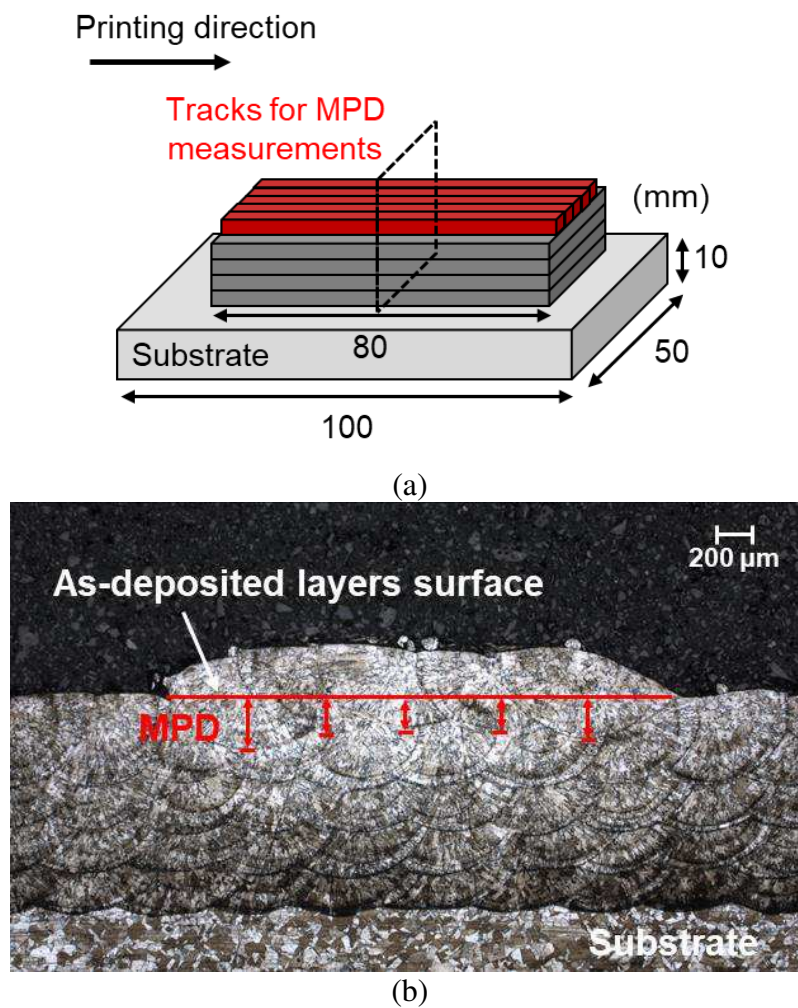


Fig. 5. Pre-test for artificial neural network (ANN) training: (a) representative pre-test specimen with four as-deposited layers and (b) melt pool depth (MPD) measurements using optical microscopy

Laser power	Number of as-deposited layers	Number of tracks
300–500 W in increments of 10 W	0–7	5
21 conditions	8 conditions	5 conditions

Table 1. Various printing conditions of the pre-test specimens

ANNs are one of the most powerful and extensively-used tools for efficiently learning complex input and output relationships without deriving mathematical equations [25]. In this study, the relationship between the MPD and the melt pool features such as the width, length, height, and slope were investigated using an ANN.

Initially, pre-tests were performed to collect data for ANN training. As shown in Table 1, the pre-test specimens were fabricated under various printing conditions using stainless steel 316L powder to generate MPDs under the influence of heat accumulation and complex melt pool geometries in multi-layer printing. Fig. 5(a) presents a representative pre-test specimen with four as-deposited layers. The as-deposited layers were composed of eight tracks on each layer. All tracks were printed in the same direction with a length of 80 mm and hatch spacing of 500 μm . With an increase in the number of as-deposited layers, a larger heat accumulation was induced.

After the fabrication of the as-deposited layers, five tracks were printed above the as-deposited layers. The melt pool width, length, height, and slope were simultaneously measured at the middle of the five tracks and used as the input for the ANN. After printing the five tracks, the middle of the specimen was cut, mounted, polished, and etched. Moreover, MD-Piano 220, MD-Largo, MD-Dac, and MD-Nap surfaces (Struers, Inc.) were used sequentially for polishing. The surface was etched using $\text{HCl}:\text{HNO}_3 = 3:1$ solution. Consequently, the MPDs were measured using optical microscopy, as shown in Fig. 5(b), and used as the output of the ANN.

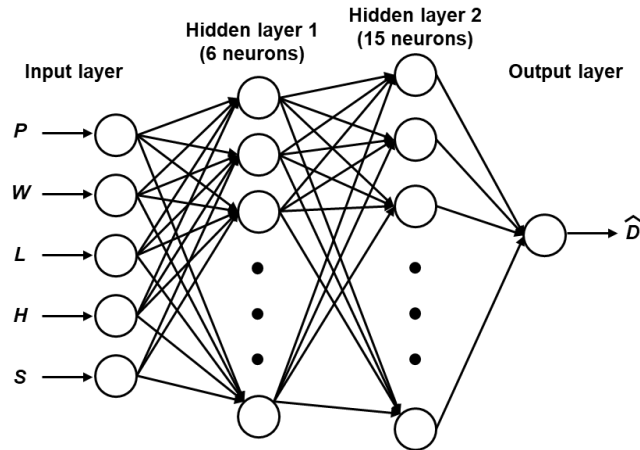


Fig. 6. The ANN model for MPD estimation

The ANN model for the estimation of the MPD from the extracted melt pool features is presented in Fig. 6. The number of data in the training dataset was 840 ($21 \times 8 \times 5$) as listed in Table 1. The laser power (P), melt pool width (W), length (L), height (H), and slope (S) were used as ANN inputs, and the MPD (D) was used as the ANN output. Subsequently, two hidden layers were used to investigate the input and output relationship with respect to the activation function of a rectified linear unit (ReLU). The number of neurons in the hidden layer were set for optimal ANN performance. A small number of neurons resulted in a low learning ability, whereas a large number of neurons increased the data processing time. After trial-and-error tests, the hidden layers with 6 and 15 neurons were determined.

In the ANN model, an Adam optimizer was used for training [26]. The model was trained over a total of 9000 epochs with an initial learning rate of 0.0002; thereafter, the learning rate was reduced by 5% in increments of 3000 epochs to improve the model convergence [27]. The training was conducted in Python (version 3.8.12) with the following central processing unit specifications: AMD Ryzen Threadripper 3990X, 64-core, RAM: 128 GB workstation environment.

From the entire training dataset, 80% of the data were used for training, 10% were used for validation, and 10% were used for test. According to the test results, as shown in Table 2, the MPD could be estimated with a root mean square error of 23 μm .

Test data	P (W)	W (μm)	L (μm)	H (mm)	S	\hat{D} (μm)	D (μm)	$\hat{D}-D$ (μm)
1	430	990	931	0.31052	-0.5647	170.4095	162	8.4095

2	500	1155	1029	0.42224	-0.42219	192.8105	196	-3.1895
3	430	1100	1029	0.28072	-0.41658	93.8576	96	-2.1424
4	400	935	931	0.30916	-0.37508	179.2374	137	42.2374
5	330	605	588	0.23813	-0.77467	164.9005	175	-10.0995
6	300	550	588	0.24637	-0.21213	118.0039	125	-6.9961
7	400	880	735	0.23986	-0.57099	112.1783	96	16.1783
8	460	1045	980	0.28214	-0.65486	145.6958	137	8.6958
9	460	1100	980	0.27897	-0.34274	180.8427	208	-27.1573
10	360	715	588	0.33909	-0.21704	180.343	212	-31.657
11	300	660	588	0.20195	-0.6659	124.4474	141	-16.5526
12	480	1100	1078	0.29834	-0.64265	112.8665	100	12.8665
13	480	1210	1029	0.26094	-0.20026	194.2018	175	19.2018
14	320	605	539	0.21816	-0.19918	188.2661	129	59.2661
15	360	825	784	0.27221	-1.2198	112.4921	100	12.4921
16	340	770	735	0.27916	-0.51621	143.0746	150	-6.9254
17	300	440	490	0.24016	-0.18394	134.6712	129	5.6712
18	350	825	735	0.27262	-0.3958	93.8577	75	18.8577
19	400	935	980	0.25308	-0.66714	136.1728	91	45.1728
20	490	1045	1078	0.27435	-0.29788	169.8057	158	11.8057
21	330	715	539	0.20778	-1.6921	196.7323	242	-45.2677
22	390	990	833	0.36547	-0.4444	113.4192	121	-7.5808
23	350	660	686	0.25607	-0.18658	152.5361	146	6.5361
24	330	715	637	0.30626	-0.4494	132.429	146	-13.571
25	480	1155	1078	0.2653	-0.42756	123.3307	104	19.3307
26	400	1100	980	0.22251	-0.28963	193.694	192	1.694
27	310	495	490	0.24534	-0.03309	168.2817	196	-27.7183
28	370	825	686	0.2421	-0.27589	99.0226	104	-4.9774
29	350	660	686	0.2438	-0.23826	135.2668	167	-31.7332
30	440	990	882	0.32656	-0.26738	132.4238	125	7.4238
31	450	990	931	0.38125	-0.24607	167.508	196	-28.492
32	440	935	882	0.25137	-0.27226	174.4505	175	-0.5495
33	490	1100	980	0.31599	-0.28884	168.0083	187	-18.9917
34	370	935	833	0.23437	-0.51806	186.378	158	28.378
35	390	880	833	0.21986	-0.07442	149.0073	137	12.0073
36	410	990	882	0.25733	-0.12469	153.5522	137	16.5522
37	320	660	637	0.18641	-0.18572	161.4759	146	15.4759
38	310	770	686	0.2495	-0.32464	121.8259	96	25.8259
39	350	660	637	0.27387	-0.20399	123.7222	96	27.7222
40	340	660	539	0.23871	-0.16824	127.8653	112	15.8653
41	420	1155	980	0.26303	-0.47603	116.0032	146	-29.9968
42	300	715	686	0.22663	-0.18124	171.7874	171	0.7874
43	380	825	784	0.23278	-0.27199	122.2266	71	51.2266
44	300	440	490	0.22377	-0.16693	147.124	187	-39.876
45	430	1045	882	0.26869	-0.19597	164.9818	137	27.9818
46	300	550	539	0.22391	-0.96903	107.6563	112	-4.3437
47	400	825	833	0.33444	-0.37893	156.0776	192	-35.9224
48	420	880	833	0.36634	-0.48638	159.585	187	-27.415
49	470	1045	931	0.34912	-0.32089	177.9499	171	6.9499

50	360	660	637	0.26353	-0.63321	128.3482	116	12.3482
51	490	1100	1029	0.3045	-0.34066	191.2989	171	20.2989
52	460	990	931	0.33645	-0.44729	176.4454	179	-2.5546
53	470	1155	1029	0.28357	-1.3269	186.7279	158	28.7279
54	390	1045	931	0.24744	-0.1375	161.8688	150	11.8688
55	490	1100	980	0.2951	-0.34721	186.3727	200	-13.6273
56	340	715	686	0.21977	-0.59377	130.2465	108	22.2465
57	370	990	882	0.23738	-0.73442	153.4126	167	-13.5874
58	350	715	735	0.29003	-0.40262	137.1979	121	16.1979
59	330	715	686	0.23479	-0.26248	128.2522	112	16.2522
60	330	715	735	0.26158	-0.2012	133.1832	121	12.1832
61	390	880	784	0.25663	-0.5827	148.6132	196	-47.3868
62	360	880	735	0.27674	-0.17504	137.6797	150	-12.3203
63	300	715	686	0.24738	-0.52832	122.2162	87	35.2162
64	320	495	588	0.29401	-0.2508	108.3034	112	-3.6966
65	470	1100	1029	0.26195	-0.2076	187.2796	192	-4.7204
66	500	1210	1078	0.22398	-0.98723	197.1733	158	39.1733
67	310	605	637	0.26863	-0.39465	120.3318	104	16.3318
68	360	770	735	0.23017	-0.14484	138.6969	108	30.6969
69	310	605	539	0.21667	-0.76212	110.4609	116	-5.5391
70	500	1100	1225	0.39967	-0.57592	213.0112	196	17.0112
71	470	1100	980	0.25351	-0.52424	182.3415	192	-9.6585
72	410	990	784	0.3163	-0.18874	151.6327	175	-23.3673
73	460	1155	980	0.28861	-0.52329	179.826	196	-16.174
74	330	715	735	0.22676	-0.37715	133.1713	96	37.1713
75	380	825	833	0.34226	-0.31069	152.0629	154	-1.9371
76	450	1045	931	0.36228	-0.41159	173.9299	192	-18.0701
77	370	935	833	0.3422	-0.20607	149.035	183	-33.965
78	470	1155	1029	0.2397	-0.45233	186.7555	225	-38.2445
79	330	715	686	0.20016	-0.64801	128.2323	129	-0.7677
80	360	880	686	0.21918	-0.39225	132.7383	91	41.7383
81	320	605	588	0.26915	-0.0303	117.4306	96	21.4306
82	300	660	588	0.22534	-0.22798	112.8868	108	4.8868
83	340	715	637	0.32544	-0.35505	125.3463	116	9.3463
84	370	825	735	0.25608	-0.24322	140.1947	154	-13.8053

Table 2. Online MPD estimation results from the ANN test data

2.3. The MPD feedback control

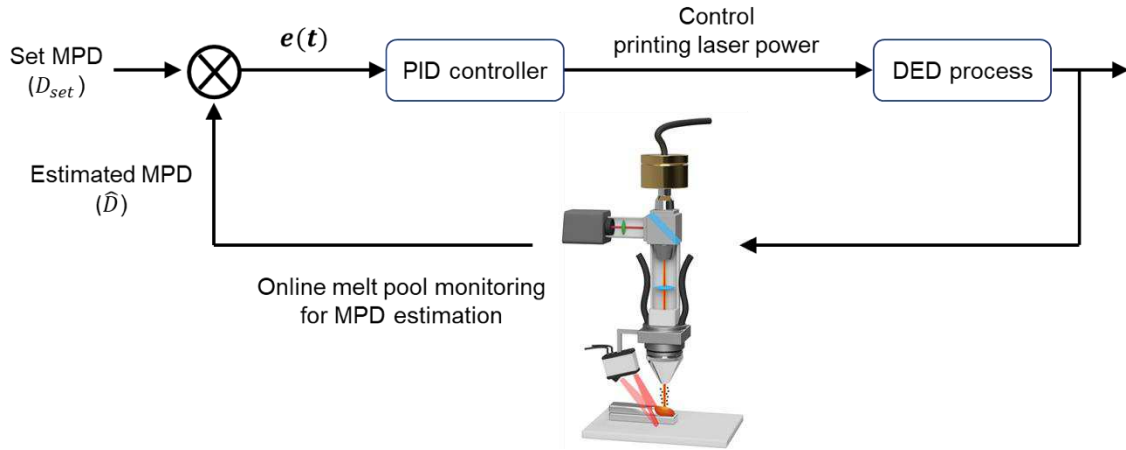


Fig. 7. Architecture of the proposed MPD feedback control system

Feedback control refers to a system in which the output is controlled using a system measurement [28]. This measurement is compared with a pre-set reference value and the difference is defined as an error. The controller generates a control input based on the error. Feedback control is required for the improvement of the part quality, to increase the product throughput, and to reduce the material waste. Several AM feedback control strategies have been reported. For example, the laser power was controlled to maintain the melt pool width to develop a more uniform microstructure [29]. Another melt pool width control system was developed using laser power modulation to control the bead geometry in real time [30, 31]. However, a control system has not been developed for porosity reduction in the DED process. The development of an MPD feedback control process is necessary to reduce the porosity and improve the overall part quality.

The proposed MPD feedback control system is presented in Fig. 7. The proposed system uses a well-known control loop mechanism, namely, a proportional–integral–derivative (PID) controller [32], to adjust the printing laser power in real time to maintain the MPD at a set value. Using the PID controller, the error value $e(t)$, which indicates the difference between the desired set value (set MPD, D_{set}) and the measured process value (estimated MPD, \hat{D}), is continuously calculated, and the laser power is adjusted according to $e(t)$. The proposed PID controller can be expressed as follows:

$$\Delta P = K_p \left(e(t) + \frac{1}{T_i} \sum e(t) + T_d \frac{e(t) - e(t-1)}{\text{sampling rate}} \right) \quad (2.1)$$

where ΔP represents the change in laser power. Before applying the PID controller, each

gain of the proportional, integral, and derivative terms was tuned. The proportional term K_p represents the current value of the $e(t)$. This term induces a significant immediate reaction on the output, thus causing the process variable to approach the set value. As $e(t)$ decreases, the influence of the proportional term on the output decreases. Thereafter, the integral term T_i accounts for previous values of $e(t)$ and integrates them over time. In general, the integral term does not have as immediate an influence on the output as the proportional term; however, this term reduces $e(t)$ in a steady state. The derivative term T_d is used to predict the future trend of $e(t)$ based on its current rate of change. Moreover, the derivative term is necessary to prevent the controller from overshooting.

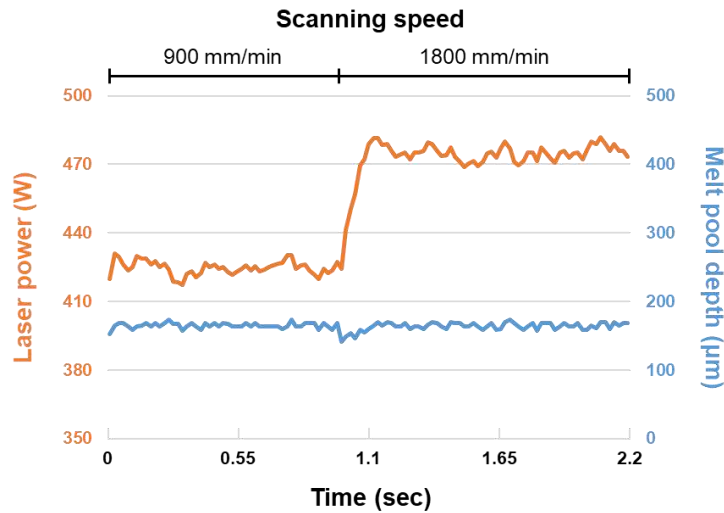


Fig. 8. Step response test for proportional–integral–derivative (PID) gain tuning

The PID gains were tuned by conducting an iterative step response test to deposit single-tracks with significant changes in the scanning speed. Fig. 8 presents the results of the step response test after tuning the PID gain. The MPD was maintained with respect to significant variations in the scanning speed.

Feedback element	K_p	T_i	T_d
Melt pool width	0.08	50	0.08
MPD	0.6	500	0.0005

Table 3. The PID gains of the proposed feedback control system

To validate the porosity reduction performance of the proposed MPD control system, a melt pool width control system was developed in the same manner. Each gain of the PID controllers is shown in Table 3. The sampling rate of the melt pool width feedback control system was 200 Hz, which is the same as the frame rate of the infrared camera. In the case of the MPD feedback control system, the sampling rate was 80 Hz, given that approximately 12 ms was required to simultaneously collect data from the infrared camera and line scanner to estimate the MPD using an ANN.

2.4. Experimental setup

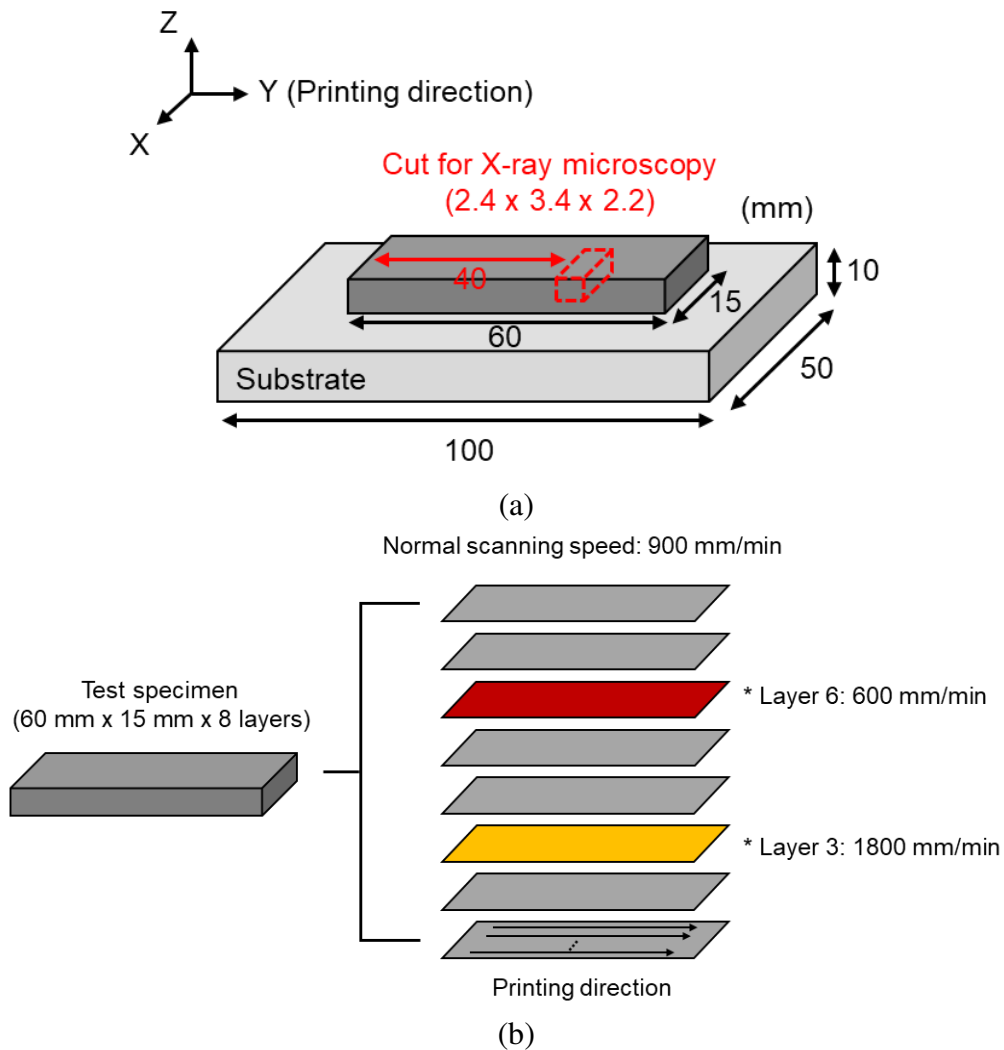


Fig. 9. (a) Description of the test specimen and (b) manually-varied scanning speed in specific layers

Control method	Set value	Controller
Uncontrolled	N/A	N/A
Energy density	0.44 W·min/mm	N/A
Melt pool width	1045 μm	PID
MPD	165 μm	PID

Table 4. Methods for laser power control

The test specimens were fabricated using stainless steel 316L material, as shown in Fig. 9(a). Each specimen was composed of eight layers with dimensions of 60 mm \times 15 mm. Each layer had 31 tracks with a hatch spacing of 500 μm and a layer height of 250 μm . The printing direction of all the tracks was the positive Y direction.

The normal laser power and scanning speed of the author's DED machine for stainless steel 316L deposition are 400 W and 900 mm/min, respectively. However, the scanning speed of two specific layers were set to abnormal values to artificially increase the porosity. The scanning speed of Layer 3 was 1800 mm/min, and the scanning speed of Layer 6 was 600 mm/min, as shown in Fig. 9(b). Higher-than-typical scanning speeds led to a decrease in the laser thermal energy delivered to the melt pool, thus resulting in a small MPD and lack of fusion in Layer 3. Conversely, lower-than-typical scanning speeds led to a large MPD and caused gas entrapment in Layer 6.

As shown in Table 4, the porosity reduction performance of the proposed MPD control system was compared with existing power control methods. Specimens were fabricated by applying each method. Initially, 400 W of constant laser power was used for fabrication. Thereafter, the laser power was adjusted to maintain the energy density (laser power/scanning speed) during printing. The set energy density was 0.44 W·min/mm, which was derived from the division of the normal laser power by the normal scanning speed. Subsequently, the laser powers of Layer 3 and Layer 6 were adjusted to 800 W and 267 W, respectively, according to the scanning speed. In the third case, the laser power was controlled using real-time feedback, to maintain the melt pool width. The set value of the melt pool width was 1045 μm , which typically occurred at the normal laser power and scanning speed. Finally, the MPD was estimated and controlled in real-time using the proposed MPD control system. Thereafter, the

laser power was adjusted to minimize the discrepancy between the estimated MPD and the set MPD. The set value of the MPD was $165\ \mu\text{m}$, which typically occurred at the normal laser power and scanning speed. Given the line scanning offset to avoid powder spatter, the first 27 mm of the tracks were not controlled using feedback.

After fabricating each specimen, a sample with a size of $2.4 \times 3.4 \times 2.2\ \text{mm}^3$ was sectioned from the top surface, as indicated by the red dotted line in Fig. 9(a). The type and degree of the generated porosity in the sample were analyzed using X-ray microscopy (Xradia 520 Versa, ZEISS Co. Ltd.) with a voxel size of $3.8\ \mu\text{m}$.

3. Results and Discussions

3.1. Results of laser power control

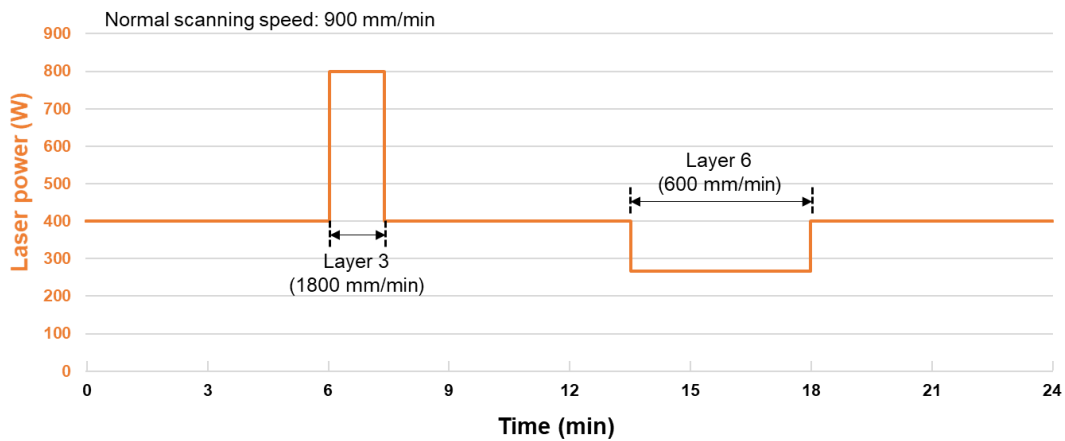


Fig. 10. Time series for laser power with energy density control

The laser power was adjusted differently to control the energy density, melt pool width, and MPD. The time series for the laser power with energy density control is shown in Fig. 10. The printing was initiated with a laser power of 400 W and scanning speed of 900 mm/min. However, the scanning speed was doubled in Layer 3, and the laser power was then increased by 800 W to maintain the energy density. In Layer 6, the scanning speed was two-thirds of the normal scanning speed, and the laser power was then reduced by 267 W. The laser power for each layer was set in advance.

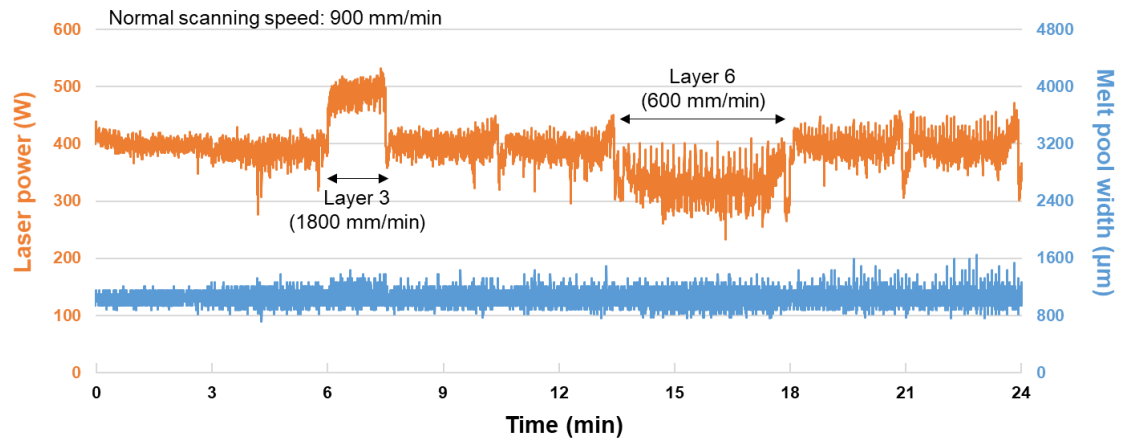


Fig. 11. Time series for laser power with melt pool width control

Fig. 11 presents the time series for the laser power with respect to melt pool width control and melt pool width measured in real time. The laser power was controlled in real time to maintain the melt pool width at $1045 \mu\text{m}$ using the PID controller. At Layers 3 and 6, the laser power was particularly changed due to the scanning speed difference. The laser power occasionally decreased at the edge of the layers, given that the heat was accumulated and the set melt pool width could be achieved at the lower laser power. The average of the melt pool width measurements was $1043 \mu\text{m}$, and the standard deviation was $74 \mu\text{m}$. Although it was difficult to control the melt pool width due to the resolution limitation of the coaxial infrared camera ($55 \mu\text{m}$), the average value was close to the set value of $1045 \mu\text{m}$.

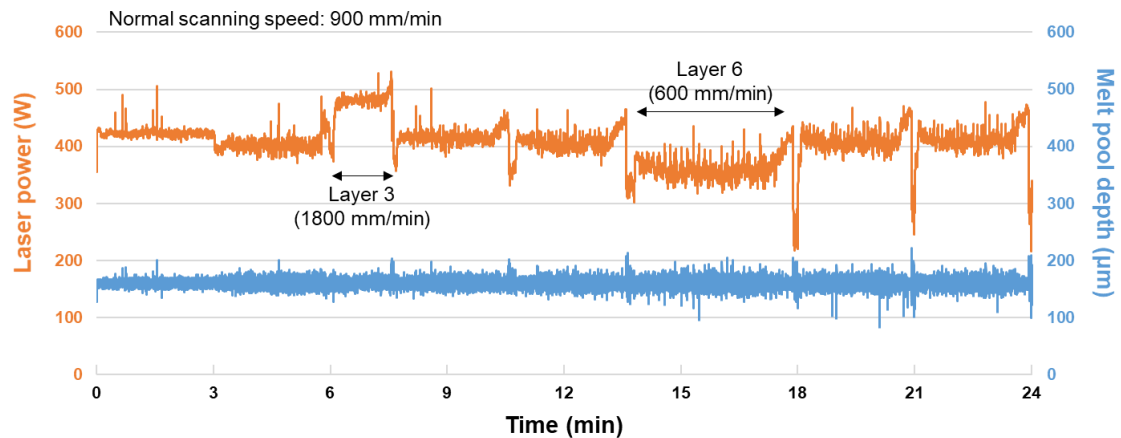


Fig. 12. Time series for laser power with MPD control

Fig. 12 presents the results of the laser power control based on the MPD estimated in real time. The PID controller was used to minimize the discrepancy between the estimated MPD

and the set MPD at 165 μm . The laser power was particularly increased in Layer 3 and decreased in Layer 6 due to the scanning speed difference. Similar to melt pool width control, the laser power decreased occasionally at the edge of the layer. However, the MPD was stably estimated with an average of 165 μm and the standard deviation of 7.79 μm .

3.2. Porosity reduction results

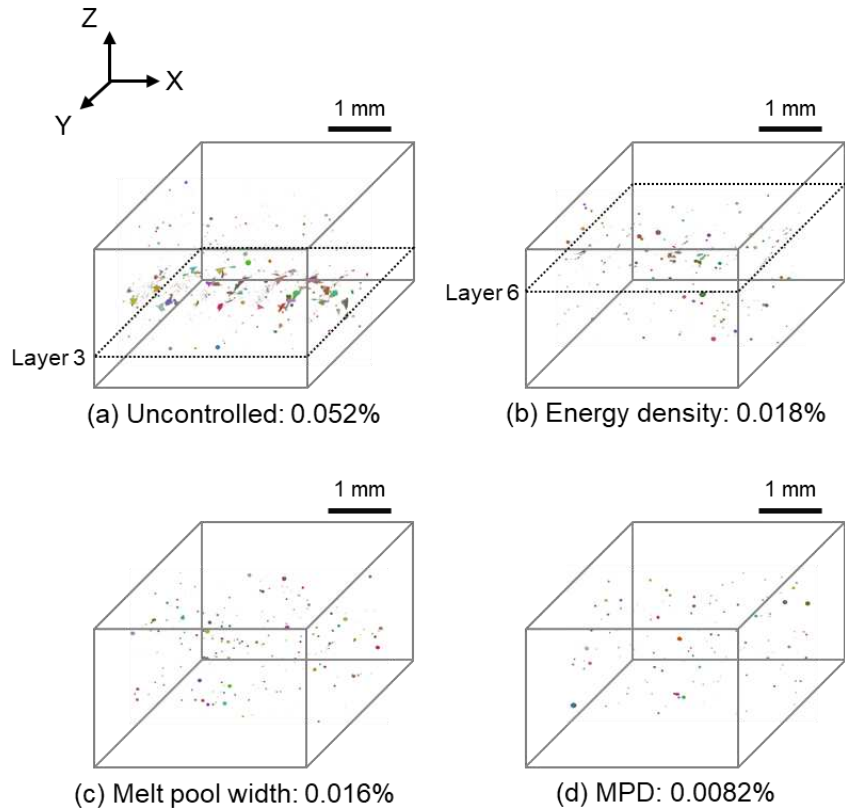
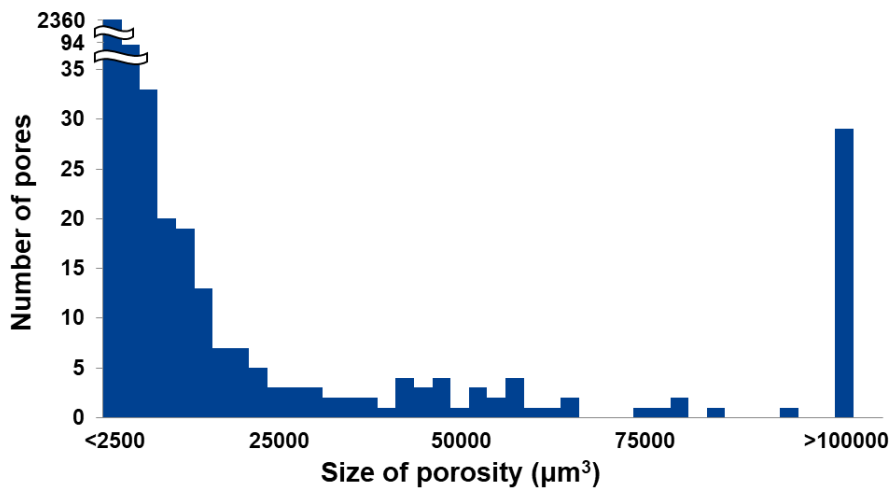


Fig. 13. Representative X-ray microscopy results for test specimens



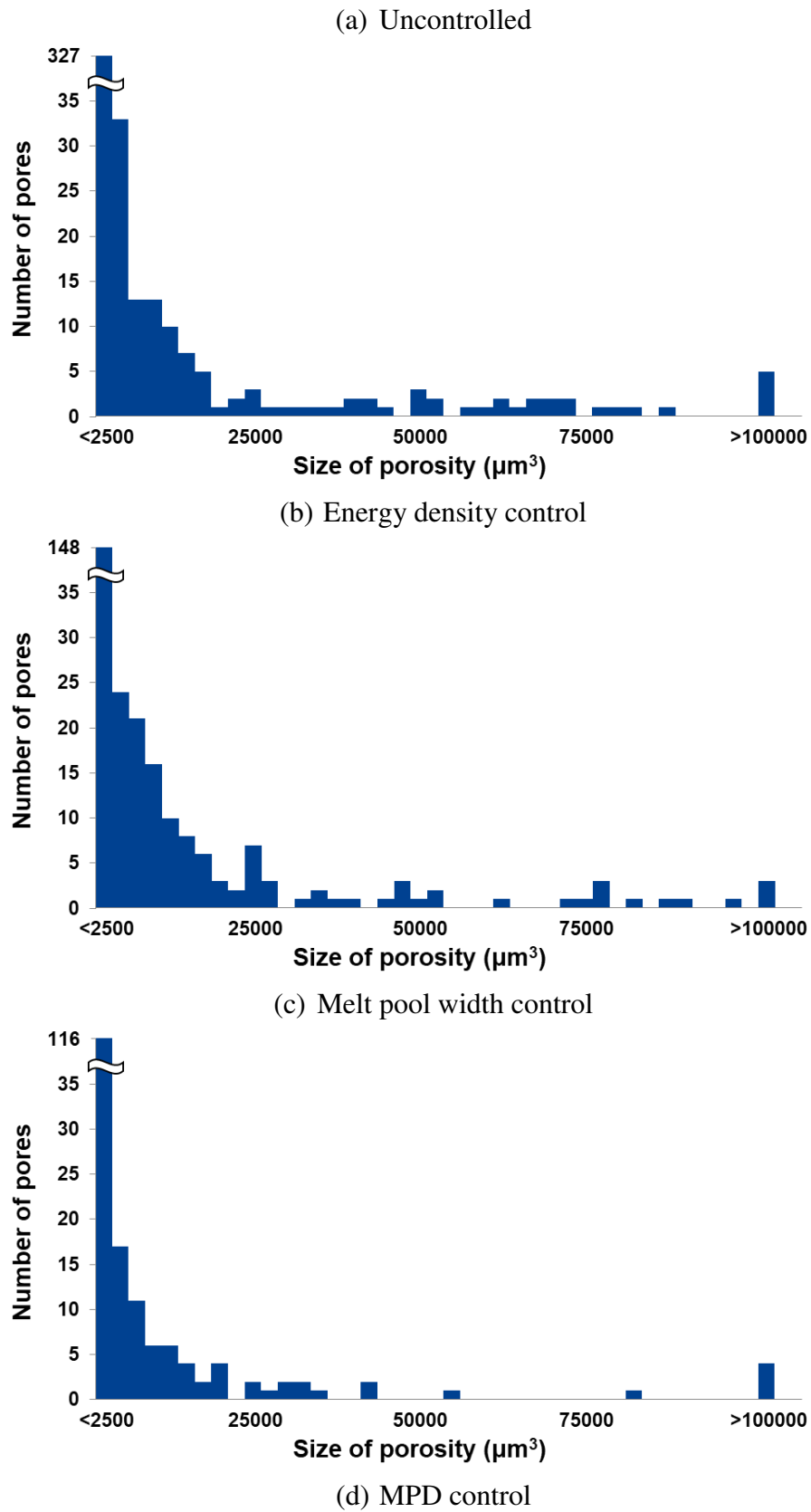


Fig. 14. Representative porosity volumetric distribution of test specimens

Fig. 13 presents the porosity of each control method investigated using X-ray microscopy.

Initially, 0.052% of porosity was generated in the sample fabricated with a constant laser power, as shown in Fig. 13(a). In Layer 3, the lack of fusion occurred along the printing direction due to the small MPD induced by a high scanning speed (1800 mm/min). Moreover, most of the gas entrapment occurred around Layer 6 due to the large MPD induced by a low scanning speed (600 mm/min). Fig. 14(a) presents the overall volumetric distribution of the porosity in the sample.

As shown in Fig. 13(b), 0.018% of porosity was observed during the control of the energy density. Compared with Fig. 14(a), the total amount of porosity decreased, as shown in Fig. 14(b). There was a significant decrease in the number of pores with volumes less than $2500 \mu\text{m}^3$ or larger than $100000 \mu\text{m}^3$, given that the lack of fusion did not occur by increasing the laser power of Layer 3 to 800 W. However, 44% of the total porosity was around Layer 6 along the printing direction. These pores were due to the lack of fusion caused by the low laser power (267 W) calculated from the energy density. The results suggest the limitation of the energy density as an indicator of porosity.

Fig. 13(c) presents the result of porosity reduction by controlling the melt pool width. In this method, 0.016% of porosity was observed in the overall sample. Compared with energy density control, the gas entrapment with dimensions of $2500 \mu\text{m}^3$ or less, significantly decreased, as presented in Fig. 14(c). This is because the laser power was adjusted to maintain the melt pool width and the gases readily escape from the melt pool.

The sample with the controlled MPD had the lowest porosity of 0.0082% when compared with the other samples. As shown in Fig. 14(d), both large and small volumes of pores were significantly reduced when compared with Fig. 14(a). This confirms that lack of fusion and gas entrapment can be reduced by controlling the MPD. The remaining porosity was distributed in the sample, regardless of the layer, which may be due to the gas contained in the powder.

Control methods for porosity reduction	Uncontrolled (%)	Energy density (%)	Melt pool width (%)	MPD (%)
Test 1	0.052	0.018	0.016	0.0082
Test 2	0.054	0.018	0.015	0.01
Test 3	0.051	0.022	0.018	0.01

Test 4	0.052	0.021	0.015	0.012
Average	0.052	0.020	0.016	0.010

Table 5. Results of porosity volume fraction using control methods

Additional tests were performed to validate the porosity reduction performance of each method. Table 5 presents the average of the porosity volume fractions obtained from the four tests. Consequently, the porosity of the samples printed with the developed MPD control system was 81% reduced in comparison with the uncontrolled samples.

4. Conclusions

In this study, a real-time MPD estimation and control system was developed for porosity reduction in the metal-DED process. Initially, the features of the melt pool were extracted from the online monitoring system, and the MPD was estimated in real time using an ANN. Thereafter, the laser power was adjusted with the developed feedback control system to maintain the MPD during the DED process. Based on the experimental results, the following conclusions were reached:

- 1) The MPD was estimated in real time with an accuracy of 23 μm using a melt pool monitoring system composed of an infrared camera, a line scanner, and an ANN.
- 2) By using a developed feedback control system, the MPD was controlled within 12 ms to minimize the discrepancy between the estimated MPD and the set MPD.
- 3) Both lack of fusion and gas entrapment were reduced using real-time MPD control.
- 4) The MPD control demonstrated the highest porosity reduction performance when compared with the energy density or melt pool width control, and the porosity decreased by approximately 81% when compared with the uncontrolled parts.

Author contribution: Ikgeun Jeon: Conceptualization, Data curation, Investigation, Writing - original draft, Writing - review & editing. Peipei Liu: Data curation, Methodology, Writing - review & editing. Hoon Sohn: Funding acquisition, Project administration, Supervision.

Funding: This work was supported by the National Research Foundation of Korea (NRF)

grant funded by the Korea government (MSIT) [grant number 2019R1A3B3067987].

Availability of data and materials: Not applicable.

Availability of code: Not applicable.

Declarations

Ethics approval: The work contains no libelous or unlawful statements, does not infringe on the rights of others, or contain material or instructions that might cause harm or injury.

Consent to participate: The authors consent to participate.

Consent for publication: The authors consent to publish.

Competing interests: The authors declare no competing interests.

References

1. Diegel O, Nordin A, Motte D (2019) Additive Manufacturing Technologies. Springer
2. Ahmed N (2019) Direct metal fabrication in rapid prototyping: A review. *J Manuf Process* 42:167–191. <https://doi.org/10.1016/j.jmapro.2019.05.001>
3. Kim H, Lin Y, Tseng TLB (2018) A review on quality control in additive manufacturing. *Rapid Prototyp J* 24:645–669. <https://doi.org/10.1108/RPJ-03-2017-0048>
4. Kurgan N (2014) Effect of porosity and density on the mechanical and microstructural properties of sintered 316L stainless steel implant materials. *Mater Des* 55:235–241. <https://doi.org/10.1016/j.matdes.2013.09.058>
5. Hardin RA, Beckermann C (2007) Effect of porosity on the stiffness of cast steel. *Metall Mater Trans A Phys Metall Mater Sci* 38 A:2992–3006. <https://doi.org/10.1007/s11661-007-9390-4>
6. Tan ZE, Pang JHL, Kaminski J, Pepin H (2019) Characterisation of porosity, density, and microstructure of directed energy deposited stainless steel AISI 316L. *Addit Manuf* 25:286–296. <https://doi.org/10.1016/j.addma.2018.11.014>
7. Tamas-Williams S, Withers PJ, Todd I, Prangnell PB (2017) The Influence of Porosity on Fatigue Crack Initiation in Additively Manufactured Titanium Components. *Sci Rep* 7:1–13. <https://doi.org/10.1038/s41598-017-06504-5>
8. Teng C, Gong H, Szabo A, et al (2017) Simulating melt pool shape and lack of fusion porosity for selective laser melting of cobalt chromium components. *J Manuf Sci Eng Trans ASME* 139:. <https://doi.org/10.1115/1.4034137>
9. Tang M, Pistorius PC, Beuth JL (2017) Prediction of lack-of-fusion porosity for powder bed fusion. *Addit Manuf* 14:39–48. <https://doi.org/10.1016/j.addma.2016.12.001>
10. Reijonen J, Revuelta A, Riipinen T, et al (2020) On the effect of shielding gas flow on porosity and melt pool geometry in laser powder bed fusion additive manufacturing. *Addit Manuf* 32:101030. <https://doi.org/10.1016/j.addma.2019.101030>

11. Kasperovich G, Hausmann J (2015) Improvement of fatigue resistance and ductility of TiAl6V4 processed by selective laser melting. *J Mater Process Technol* 220:202–214. <https://doi.org/10.1016/j.jmatprotec.2015.01.025>
12. Vilaro T, Colin C, Bartout JD (2011) As-fabricated and heat-treated microstructures of the Ti-6Al-4V alloy processed by selective laser melting. *Metall Mater Trans A Phys Metall Mater Sci* 42:3190–3199. <https://doi.org/10.1007/s11661-011-0731-y>
13. Shipley H, McDonnell D, Culleton M, et al (2018) Optimisation of process parameters to address fundamental challenges during selective laser melting of Ti-6Al-4V: A review. *Int J Mach Tools Manuf* 128:1–20. <https://doi.org/10.1016/j.ijmachtools.2018.01.003>
14. Gong H, Rafi K, Gu H, et al (2015) Influence of defects on mechanical properties of Ti-6Al-4V components produced by selective laser melting and electron beam melting. *Mater Des* 86:545–554. <https://doi.org/10.1016/j.matdes.2015.07.147>
15. Kumar P, Jano F, Javed A, et al (2019) Influence of laser processing parameters on porosity in Inconel 718 during additive manufacturing. *Int J Adv Manuf Technol* 103:1497–1507
16. Kasperovich G, Haubrich J, Gussone J, Requena G (2016) Erratum: Corrigendum to “Correlation between porosity and processing parameters in TiAl6V4 produced by selective laser melting” (*Materials and Design* (2016) 105 (160–170)). *Mater Des* 112:160–161. <https://doi.org/10.1016/j.matdes.2016.09.040>
17. Tamas-Williams S, Withers PJ, Todd I, Prangnell PB (2016) The Effectiveness of Hot Isostatic Pressing for Closing Porosity in Titanium Parts Manufactured by Selective Electron Beam Melting. *Metall Mater Trans A Phys Metall Mater Sci* 47:1939–1946. <https://doi.org/10.1007/s11661-016-3429-3>
18. Liverani E, Lutey AHA, Ascari A, Fortunato A (2020) The effects of hot isostatic pressing (HIP) and solubilization heat treatment on the density, mechanical properties, and microstructure of austenitic stainless steel parts produced by selective laser melting (SLM). *Int J Adv Manuf Technol* 107:109–122. <https://doi.org/10.1007/s00170-020-05072-9>
19. Fetzer F, Sommer M, Weber R, et al (2018) Reduction of pores by means of laser

- beam oscillation during remote welding of AlMgSi. *Opt Lasers Eng* 108:68–77.
<https://doi.org/10.1016/j.optlaseng.2018.04.012>
20. Gong M, Meng Y, Zhang S, et al (2020) Laser-arc hybrid additive manufacturing of stainless steel with beam oscillation. *Addit Manuf* 33:101180.
<https://doi.org/10.1016/j.addma.2020.101180>
 21. Goossens LR, Van Hooreweder B (2021) A virtual sensing approach for monitoring melt-pool dimensions using high speed coaxial imaging during laser powder bed fusion of metals. *Addit Manuf* 40:101923.
<https://doi.org/10.1016/j.addma.2021.101923>
 22. Hummel M, Kulkens M, Schöler C, et al (2021) In situ X-ray tomography investigations on laser welding of copper with 515 and 1030 nm laser beam sources. *J Manuf Process* 67:170–176. <https://doi.org/10.1016/j.jmapro.2021.04.063>
 23. Guo Q, Zhao C, Qu M, et al (2019) In-situ characterization and quantification of melt pool variation under constant input energy density in laser powder bed fusion additive manufacturing process. *Addit Manuf* 28:600–609.
<https://doi.org/10.1016/j.addma.2019.04.021>
 24. Cioboata D, Traistaru F, Abalaru A, et al (2011) Equipments for high precision measurement of free form surfaces micro and macro geometry. *Rom Rev Precis Mech Opt Mechatronics* 257–261
 25. Agatonovic-Kustrin S, Beresford R (2000) Basic concepts of artificial neural network (ANN) modeling and its application in pharmaceutical research. *J Pharm Biomed Anal* 22:717–727. [https://doi.org/10.1016/S0731-7085\(99\)00272-1](https://doi.org/10.1016/S0731-7085(99)00272-1)
 26. Kingma DP, Ba JL (2015) Adam: A method for stochastic optimization. *3rd Int Conf Learn Represent ICLR 2015 - Conf Track Proc*
 27. Darken C, Chang J, Moody J (1992) Learning rate schedules for faster Stochastic gradient search. In: *Neural Networks for Signal Processing - Proceedings of the IEEE Workshop*. Citeseer, pp 3–12
 28. Firoozian R (2014) *Feedback Control Theory Continued*. Courier Corporation
 29. Akbari M, Kovacevic R (2019) Closed loop control of melt pool width in robotized

- laser powder-directed energy deposition process. *Int J Adv Manuf Technol* 104:2887–2898. <https://doi.org/10.1007/s00170-019-04195-y>
30. Wang Y, Lu J, Zhao Z, et al (2021) Active disturbance rejection control of layer width in wire arc additive manufacturing based on deep learning. *J Manuf Process* 67:364–375. <https://doi.org/10.1016/j.jmapro.2021.05.005>
 31. Xia C, Pan Z, Zhang S, et al (2020) Model predictive control of layer width in wire arc additive manufacturing. *J Manuf Process* 58:179–186. <https://doi.org/10.1016/j.jmapro.2020.07.060>
 32. Willis MJ (1999) Proportional-integral-derivative control. Dept Chem Process Eng Univ Newcastle